The Western Eurasian Basin Halocline in 2017: Insights From Autonomous NO Measurements and the Mercator Physical System

Cécilia Bertosio, Christine Provost, Nathalie Sennéchael, Camila Artana, Marylou Athanase, Elisabeth Boles, Jean-Michel Lellouche, Gilles Garric

JGR Oceans

RESEARCH ARTICLE
10.1029/2020JC016204

The Western Eurasian Basin Halocline in 2017: Insights From Autonomous NO Measurements and the Mercator Physical System

Cécilia Bertosio[1], Christine Provost[1], Nathalie Sennéchael[1], Camila Artana[2], Marylou Athanase[1], Elisabeth Boles[1,3], Jean-Michel Lellouche[2], and Gilles Garric[2]

[1]Laboratoire LOCEAN-IPSL, Sorbonne Université (UPMC, Univ. Paris 6), CNRS, IRD MNHN, Paris, France, [2]MERCATOR OCEAN, Parc Technologique du Canal, Ramonville Saint Agne, France, [3]Now at Environmental Fluid Mechanics Laboratory, Stanford University, Stanford, CA, USA

Key Points:
- First profiles of the NO parameter from an autonomous ice-tethered buoy in the Arctic Ocean documented the halocline in 2017
- In Nansen Basin, a NO minimum on the 27.8 σ-horizon traced the deepest winter mixed layer and lower halocline waters
- In the transpolar drift, a smaller NO minimum on the 27.4 σ-horizon (cold halocline) was traced back to the East Siberian Seas

Correspondence to:
C. Bertosio,
cecilia.bertosio@locean-ipsl.upmc.fr

Citation:
Bertosio, C., Provost, C., Sennéchael, N., Artana, C., Athanase, M., Boles, E., et al. (2020). The western Eurasian Basin halocline in 2017: Insights from autonomous NO measurements and the Mercator physical system. *Journal of Geophysical Research: Oceans*, *125*, e2020JC016204. https://doi.org/10.1029/2020JC016204

Received 4 MAR 2020
Accepted 18 JUN 2020
Accepted article online 23 JUN 2020

Abstract We present the first sensor-based profiles of the quasi-conservative NO parameter obtained with an autonomous ice-tethered buoy in the Arctic Ocean. Data documented the halocline in the Transpolar Drift and Nansen Basin in 2017. A NO minimum was found in the Nansen Basin on a σ-horizon of 27.8 kg·m^{-3} corresponding to the lower halocline, while a lower NO minimum of 380 μM straddled the 27.4 σ-horizon and marked the cold halocline in the Transpolar Drift. Back trajectories of water parcels encountered along the buoy drift were computed using the Mercator physical system. They suggested that waters within the NO minimum at 27.4 kg·m^{-3} could be traced back to the East Siberian Sea continental. These trajectories conformed with the prevailing positive phase of the Arctic Oscillation. The base of the lower halocline, at the 27.85 σ-horizon, corresponded to the density attained in the deepest winter mixed layer north of Svalbard and cyclonically slowly advected from the slope into the central Nansen Basin. The 27.85 σ-horizon is associated with an absolute salinity of 34.9 g·kg^{-1}, a significantly more saline level than the 34.3 psu isohaline commonly used to identify the base of the lower halocline. This denser and more saline level is in accordance with the deeper winter mixed layers observed on the slopes of Nansen Basin in the last 10 years. A combination of simulations and NO parameter estimates provided valuable insights into the structure, source, and strength of the Arctic halocline.

Plain Language Summary Dissolved oxygen and nitrate data, measured for the first time by an autonomous ice-tethered profiler in the Arctic Ocean, were combined to compute the NO parameter, a tracer useful for differentiating oceanic water masses. Together with ocean and sea ice model simulations, the spatial distribution of this NO parameter provided valuable insights into the structure and sources of the water in the central Arctic. The halocline, a layer near the surface where salinity increases rapidly with depth, isolates sea ice from the heat stored in the salty Atlantic water below. Waters in the halocline could be traced back to two different sources: the East Siberian Sea continental slope and the slope north of Svalbard where deep winter convection is important. Additionally, our analyses show that previous definitions of the bounds of the halocline layer no longer apply, likely because of increasing influence of saltier Atlantic water near the surface.

1. Introduction

The halocline, a subsurface layer with increasing salinity with depth, is a fundamental structure of the upper Arctic Ocean. The halocline acts as an insulating barrier separating the cold and fresh surface mixed layer (SML) and sea ice from the warm and salty Atlantic water (AW) below: hence, it is a key feature in the maintenance of the sea ice cover (e.g., Steele & Boyd, 1998). The Arctic Ocean halocline is complex, consisting of several water masses and source regions. The halocline can be divided into lower, cold, and upper halocline layers. The lower halocline waters (LHW) are formed via freshening, cooling, and mixing of AW with sea ice melt water upon entry in the Arctic north of Svalbard or the Barents Sea (Rudels et al., 1996). In the LHW, temperature and salinity ($34 < S < 34.5$) increase with depth until the upper limit of the warm and salty AW. The cold halocline waters, characterized with homogeneous near-freezing temperatures and large vertical salinity gradient ($33 < S < 34$), result from additional influences from the Kara, Laptev, and/or East Siberian Sea (Alkire et al., 2017; Rudels et al., 2004; Steele & Boyd, 1998). The upper halocline waters

(UHW) are made of fresher Pacific-derived contributions overriding the denser Atlantic-origin halocline waters. UHW are mainly found in the Amerasian Basin, and their horizontal extent and incursion in the Eurasian Basin vary between years, mainly depending on the position of the Transpolar Drift (TPD; e.g., Alkire et al., 2019; Anderson et al., 2013). Observational activities in the Canada Basin have revealed that UHW had a complex structure resulting from the distinct water sources (Alkire et al., 2010; Shimada et al., 2005), the different paths traveled on the shelves (Bourgain et al., 2013; Steele et al., 2004), and from variable seasonal ventilation (Timmermans et al., 2017).

The halocline strength, that is, its stratification, shows large interannual and spatial variations (e.g., Bourgain & Gascard, 2011; Polyakov et al., 2018). Nevertheless, trends are clear, and since 1981, there is a contrasted evolution in the strength of the Arctic halocline with an increasing stratification in the Amerasian Basin and a weakening in the Eurasian Basin (Polyakov et al., 2018). These changes are concomitant with the progression of AW signature from the western Eurasian Basin to the eastern Eurasian Basin, called "Atlantification" (Polyakov et al., 2017). The major driver for these changes is a powerful combination of processes associated with declining sea ice cover and weakening of stratification in the layers over the AW leading to an increase in winter convection depth.

Tracers (isotopes and nutrients) have proven very useful in helping to identify variations in sources of the water masses composing the halocline in the Central Arctic and suggesting circulation patterns (e.g., Alkire et al., 2007, 2015). In particular, the NO parameter, a semiconservative tracer combining nitrate and dissolved oxygen (DO), has been used to trace water masses at depths and below the active layer of mixing. Defined as $NO = 9 \times [NO_3] + [O_2]$ (Broecker, 1974), it exhibits a minimum in the lower halocline (Jones & Anderson, 1986) that is consistent with a convective formation of LHW in the western Eurasian Basin (Rudels et al., 1996). Sensor-based observations yielding high-resolution vertical profiles of the NO parameter displayed another NO minimum in the upper halocline in the Makarov Basin in 2007 and 2008. This NO minimum was indicative of a ventilation source, most likely from Siberian shelves, not present in the Amundsen Basin (Alkire et al., 2010). Recently, it was shown that significant contrasts in the NO parameter help identify the front separating UHW contributions from Atlantic (lower NO) and Pacific (higher NO) waters in the Central Arctic Ocean in summer 2015 (Alkire et al., 2019).

If the NO parameter has proven to be a useful qualitative tracer of halocline waters from the Amerasian Basin and LHW from the Eurasian Basin, inferring routes and time scales from NO distribution is speculative. Sea ice back trajectories have been used for interpreting the origin and path of the mixed layer waters (e.g., Kipp et al., 2018). However, the circulation of surface and halocline waters (upper and a fortiori lower) may not necessarily be coupled (Alkire et al., 2007). Indeed, observations and numerical models show significant velocity shear in the upper layers.

We examine the NO parameter distribution in the halocline of the western Eurasian Basin in 2017 making use of the first sensor-based profiles of the NO parameter gathered with an autonomous ice-tethered platform in the Arctic Ocean. We also examine how an ocean-sea ice operational system can help interpret the observed NO distribution. The data were gathered during an 8-month drift of IAOOS23 platform from the North Pole to Fram Strait in 2017 along a meandering path across the western Eurasian Basin (Provost et al., 2017; Figure 1a). High colored dissolved organic matter (CDOM) fluorescence values and low nitrate concentrations in the upper layer (Figures 1b and 1c) were associated with water masses coming from Siberian shelves and carried with the TPD across the Central Arctic (Athanase et al., 2019). Several mesoscale structures were observed in the halocline and in the Atlantic warm layer (HE1, HE2, HE3, AW1, and AW2 in Figures 1c and 1d), and Mercator Ocean operational system helped interpret the origin of the observed mesoscale structures (Athanase et al., 2019). The data also documented two under-ice blooms: an early spring bloom in Amundsen Basin consisting of small, potentially mixotrophic phytoplankton and a summer bloom in Nansen Basin which contained a greater diversity of planktonic size classes (Boles et al., 2020).

The paper is organized as follows. Section 2 describes the in situ data focusing on the NO parameter, methods for halocline depth and strength estimates, and the Mercator Ocean operational system. Section 3 presents a NO-focused upper layer hydrography, while section 4 focuses on halocline structure, sources, and strength making use of the operational system. Section 5 discusses water mass source inferences and comparisons with previous studies. Section 6 highlights major findings and puts the work into perspective.

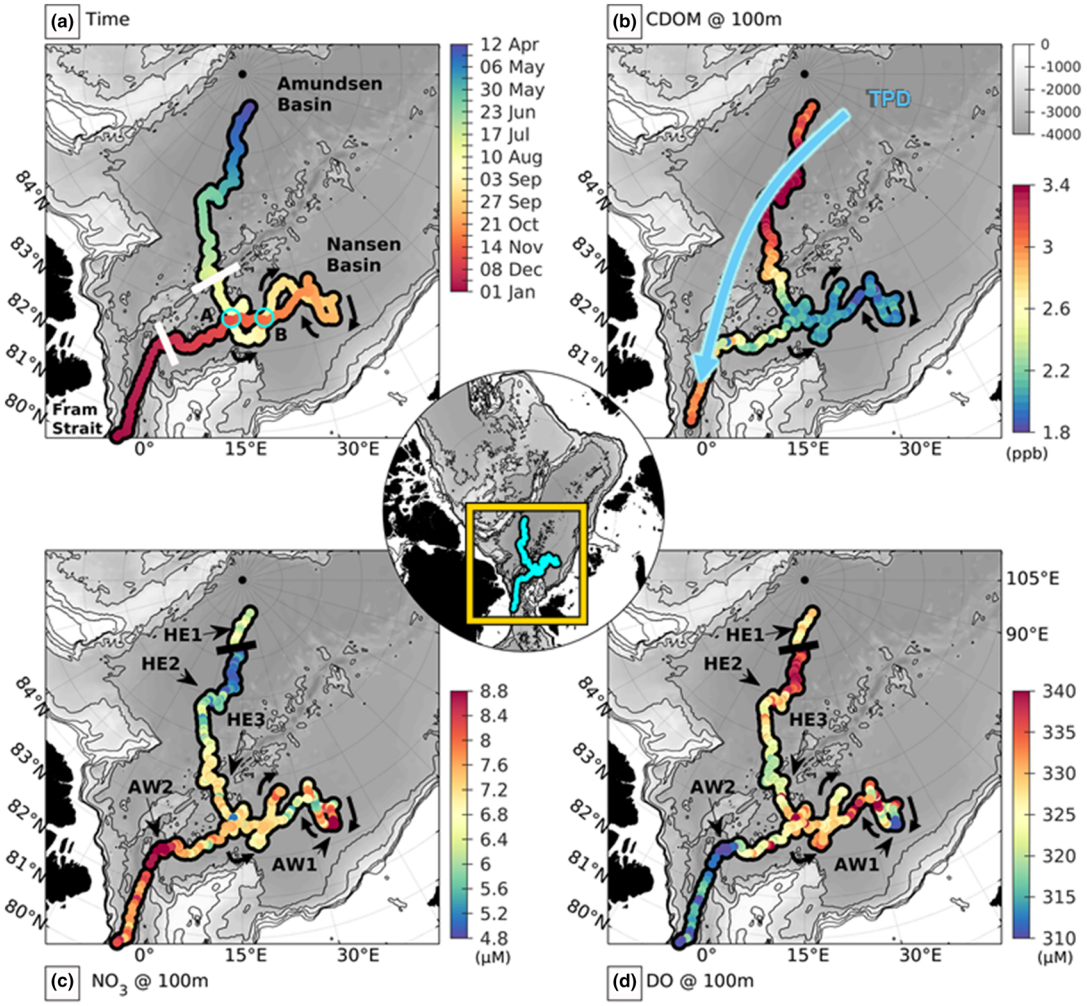

Figure 1. Along the trajectory in color: (a) date; blue circles highlight crossover points A and B; white segments delimit boundaries between basins; small black arrows mark the direction of the platform drift. (b) Colored dissolved organic matter fluorescence (CDOM, ppb) at 100 m; blue arrow sketches the transpolar drift (TPD) characterized with CDOM > 3 ppb; (c) NO_3 (μM) at 100 m and (d) dissolved oxygen (DO, μM) at 100 m. Three halocline eddies (HE) and two Atlantic water mesoscale structures (AW) are labeled. Background is bathymetry in gray scale with isolines at 500, 1,000, 2,000 and 3,200 m. The black solid line at 88.2°N indicates a frontal zone.

2. Data and Methods

2.1. Upper Ocean Data and NO Parameter

To avoid redundancy with previous works, we briefly recall the data used here and refer the reader to the description of the experimental setup and data processing in Athanase et al. (2019). The unique 8-month-long data set used here consists of a total of 431 profiles of temperature, salinity, and DO and 427 profiles of CDOM fluorescence and nitrate concentration (upper 250 m from IAOOS23 profiler; Table 1 in Athanase et al., 2019). After data processing, quality control, and interpolation, conservative temperature (CT), absolute salinity (SA), and DO data have 0.5 m vertical resolution and an accuracy of 0.005°C, 0.02 g·kg^{-1}, and 2.5 μM, respectively. NO_3 data have a 1 db vertical resolution and a 2 μM accuracy (see Appendix A), and CDOM data have a 1 db vertical resolution and a manufacturer accuracy of ±0.28 ppb (Athanase et al., 2019; Boles et al., 2020) (Figure 2).

Measurements of DO and nitrates were interpolated and combined to compute the NO parameter ($NO = 9 \times [NO_3] + [O_2]$) with a 1 db vertical resolution. A conservative uncertainty on absolute values of the NO estimates is about ±10 μM. NO values range from 375 to 410 μM, a range comparable to estimates

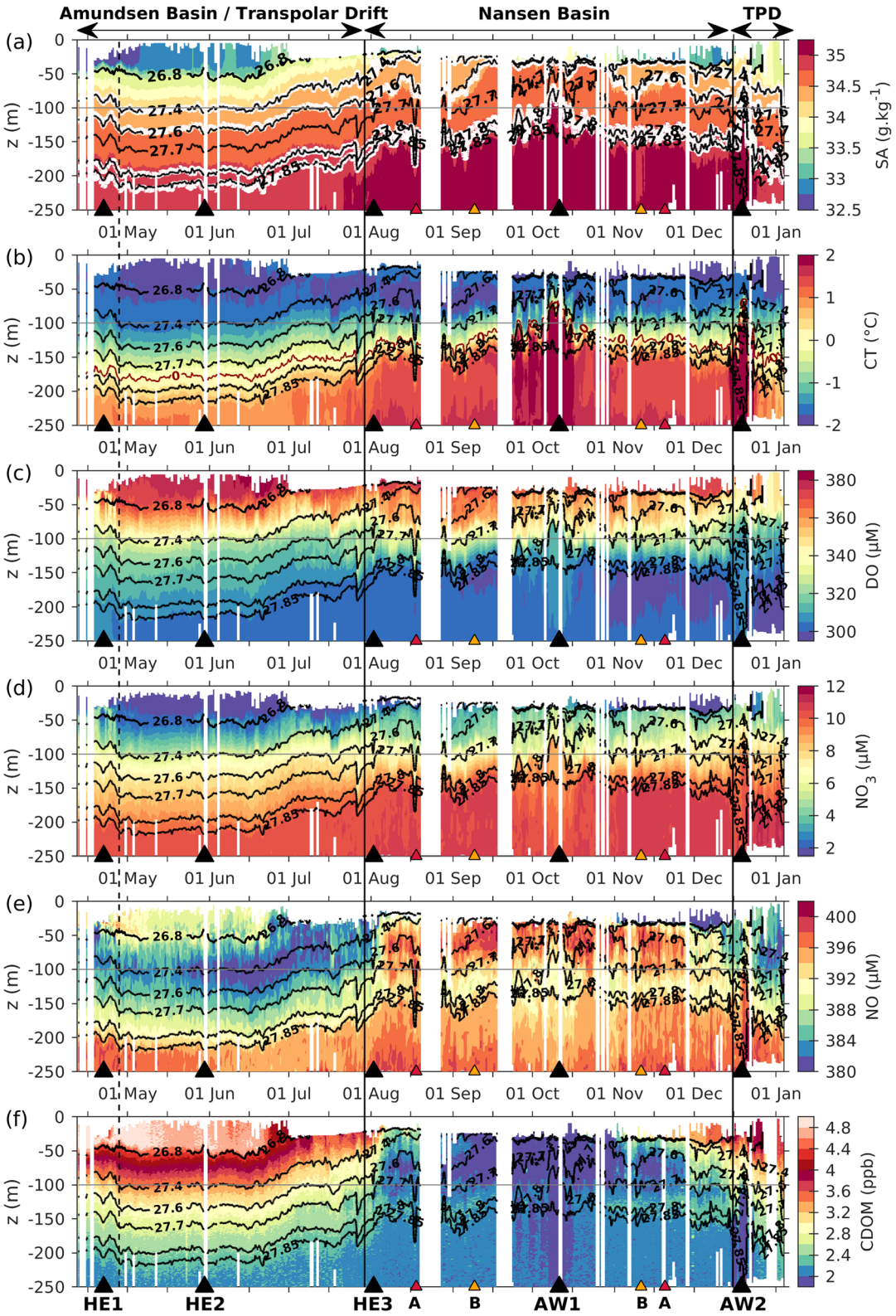

Figure 2. Hydrographic variables along the trajectory (*x* axis is time, and *y* axis is depth): (a) absolute salinity (SA, g·kg^{-1}) with isohalines 34.2, 34.46, 34.8, and 34.9 g·kg^{-1} in white; (b) conservative temperature (CT, °C) with 0°C temperature isoline in purple; (c) dissolved oxygen concentration (DO, µM); (d) nitrate concentration (NO_3, µM); (e) NO parameter (µM); and (f) colored dissolved organic matter fluorescence (CDOM, ppb). Black lines depict density isolines from 26.8 to 27.9 kg·m^{-3}. Vertical black lines delimit boundaries between basins. The dashed vertical line indicates the position of a frontal zone at 88.2°N. Positions of HE1, HE2, HE3, AW1, AW2, and two crossover points A and B are marked at the bottom.

from Alkire et al. (2010, 2017) in the Central Arctic (see Appendix A) and show a consistent distribution in space and time (Figure A2).

2.2. Halocline Definition and Characterization From Physical Parameters

The upper limit of the halocline, or depth of the SML (H_{SML}), coincides with a strong maximum in the Brunt-Väisälä frequency N^2 (Figure 4a in Athanase et al., 2019). Note that several profiles did not reach the near surface as a strong stratification at the base of the summer mixed layer, at about 30-m depth, probably impeded the ascent of the profiler, particularly in July–August 2017.

Several definitions for the depth of the lower halocline boundary (H_{halo}) can be found in the literature. Rudels et al. (1996) estimated H_{halo} as the depth of the 34.3 psu isohaline (i.e., SA = 34.46 g·kg^{-1}) as the 34.3 value appeared to be the maximum salinity reached by the winter mixed layer north of Svalbard. Bourgain and Gascard (2011) defined H_{halo} as the depth where the density ratio R_ρ ($R_\rho = \alpha\partial_z CT/\beta\partial_z SA$, where α is the thermal expansion coefficient and β the haline contraction) had a value of 0.05. The choice of threshold in SA or R_ρ for estimating the halocline depth is discussed in section 5 in light of the hydrographic measurements including NO.

The halocline thickness is then defined as $\Delta H_{halo} = H_{halo} - H_{SML}$. To measure the halocline strength, that is, its stratification, we used the available potential energy (APE), an indicator proposed by Polyakov et al. (2018), with APE$=\int_{z1}^{z2} g(\rho - \rho_{ref})z\mathrm{d}z$, where z_2 is the surface, z_1 the depth of the halocline base H_{halo}, g the gravity acceleration, ρ_{ref} is potential density at the base of the halocline, and z is depth.

Profiler observations are not Lagrangian as the platform drifted with the ice rather than the ocean, and we used model outputs to investigate possible water parcel paths and time scales.

2.3. Mercator Ocean Operational System and Satellite-Derived Products

The global Mercator Ocean operational system PSY4V3R1 (hereafter PSY4) was developed for the Copernicus Marine Environment Monitoring Service (http://marine.copernicus.eu) with a (1/12)° horizontal resolution and 50 vertical z levels with typically 1 m resolution at the surface decreasing to 450 m at the bottom and 22 levels within the upper 100 m. A full description of the system components is available in Lellouche et al. (2018). PSY4 only simulates physical variables and no biogeochemical variables. Skills of PSY4 in reproducing physical variables (sea ice, temperature, salinity, and ocean currents) in the western Eurasian Basin have been assessed in Koenig, Provost, Sennéchael, et al., 2017, Koenig, Provost, Villacieros-Robineau, et al., 2017, Ivanov et al. (2018), and Athanase et al. (2019). In particular, daily Mercator Ocean system temperature and salinity profiles show a general agreement with a well-positioned 27.8 isopycnal with adequate salinities (within 0.05) and temperatures (within 0.3°C) (Figure 10 in Athanase et al., 2019).

We used daily horizontal model velocities to investigate possible origins of water parcels encountered in the halocline during the drift. Lagrangian backward and forward trajectories of synthetic particles were tracked using a simple prediction-correction scheme similar to that employed by Fillipi et al. (2010).

Mean velocities over year 2017 at the surface (sea ice) and at 50 and 220m depth in the ocean show a common pattern with a swift drift from the East Siberian Sea toward the North Pole as well as a slower drift from the Laptev Sea toward the North Pole (Figures 3a–3c). Note the small scale of spatial structures in ocean mean velocities (Figures 3b and 3c).

Back trajectories of the modeled ice followed the platform trajectory, thus showing the reliability of Mercator ice drift (Figure 3d). They suggested that the ice floe originated from the Laptev Sea in October–November 2015 and was 1.5 years old when the IAOOS platform was installed. Back trajectories calculated from satellite-derived ice drift (doi: 10.5067/INAWUWO7QH7B) provided the same result (not shown). Sources and time scales of advection of halocline water parcels are examined in section 4.

3. NO-Focused Upper Layer Hydrography

Athanase et al. (2019) and Boles et al. (2020) documented general hydrography and biology, respectively, from the same data set. For the sake of completeness and clarity, we complemented new sections of DO

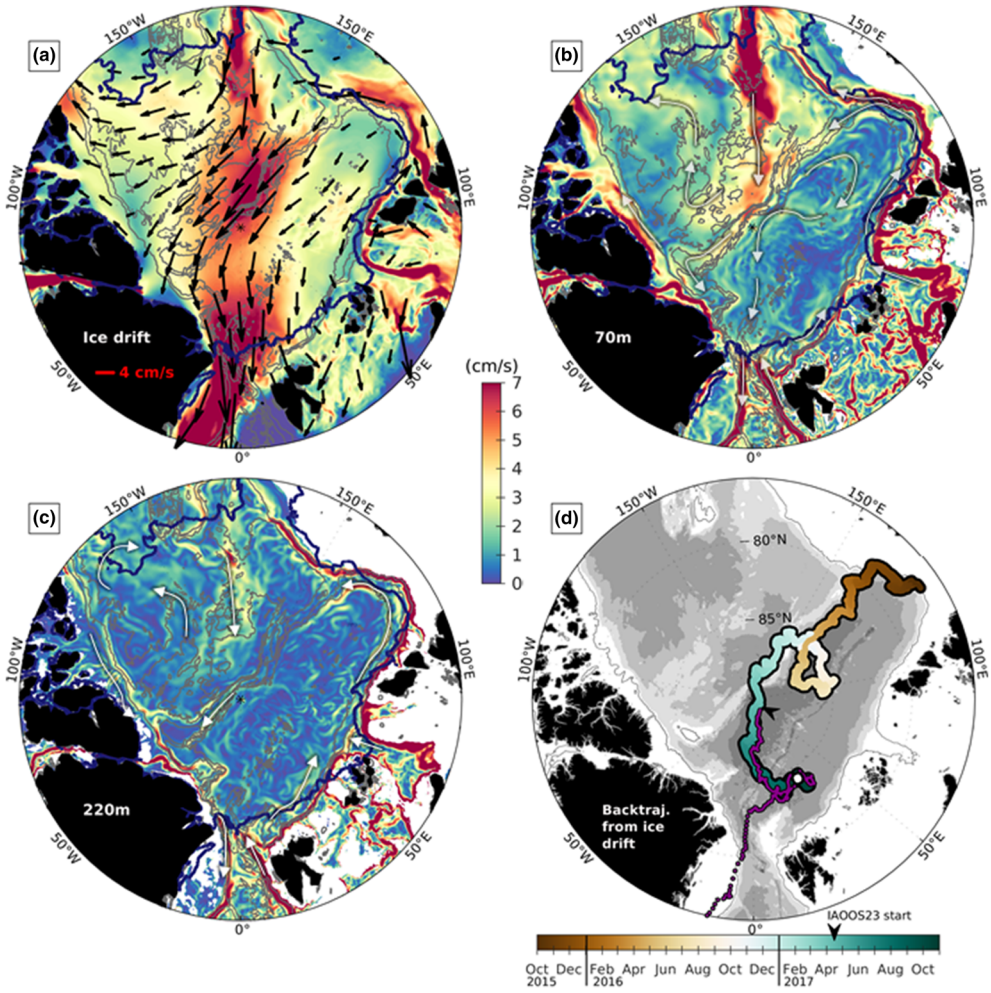

Figure 3. (a) Sea ice horizontal velocities averaged over 2017 from PSY4 outputs. Velocity amplitude in the background with a 1/12° spatial resolution, arrows subsampled every 40 grid cells for the sake of clarity. (b) Amplitude of mean ocean horizontal velocities in 2017 at 70 m (b) and 220 m (c) from PSY4 outputs. The three maps have the same color bar. The 100% ice cover limit in 2017 is shown in dark blue in (a)–(c). White arrows in (b) and (c) sketch current direction. (d) Back trajectory (color scale is time) from IAOOS23 ice floe using PSY4 sea ice velocities; the white dot is the back trajectory starting point from late October 2017; purple line is IAOOS23 trajectory.

and NO with sections of CT, SA, NO_3, and CDOM previously shown in Athanase et al. (2019) and Boles et al. (2020) (Figure 2).

Waters in the TPD (sampled in Amundsen Basin and Fram Strait) were less saline, colder, and lighter than those sampled in Nansen Basin. The mixing lines between AW and lower salinity, near-freezing surface layers, had a steeper slope in Nansen Basin than in the TPD (Figure 4a). The contrasting bends in the CT-SA curves separating near-surface and Atlantic waters illustrate the distinct stratifications in the TPD and Nansen Basin upper water columns (Figure 4a). In the TPD, the bend above the mixing line between AW and SML in the wide SA range 33.5–34.9 ($26.8 < \sigma < 27.85$ kg·m^{-3}) reflects low-salinity, river/shelf water input (Kikuchi et al., 2004). In contrast, the sharp bend below the mixing line from profiles in Nansen Basin indicates convectively formed waters with a reduced range of salinity and density ($34.3 < SA < 34.9$ g·kg^{-1} and $27.5 < \sigma < 27.85$ kg·m^{-3}).

DO concentration varied from relatively high near-surface values close to saturation level (from 390 to 345 μM varying with CT) to a minimum of 305 to 295 μM at SA of 34.9 g·kg^{-1} ($27.8 < \sigma < 27.85$ kg·m^{-3}) (Figures 2c and 4b). In contrast, nitrate concentrations were small near the surface with values below

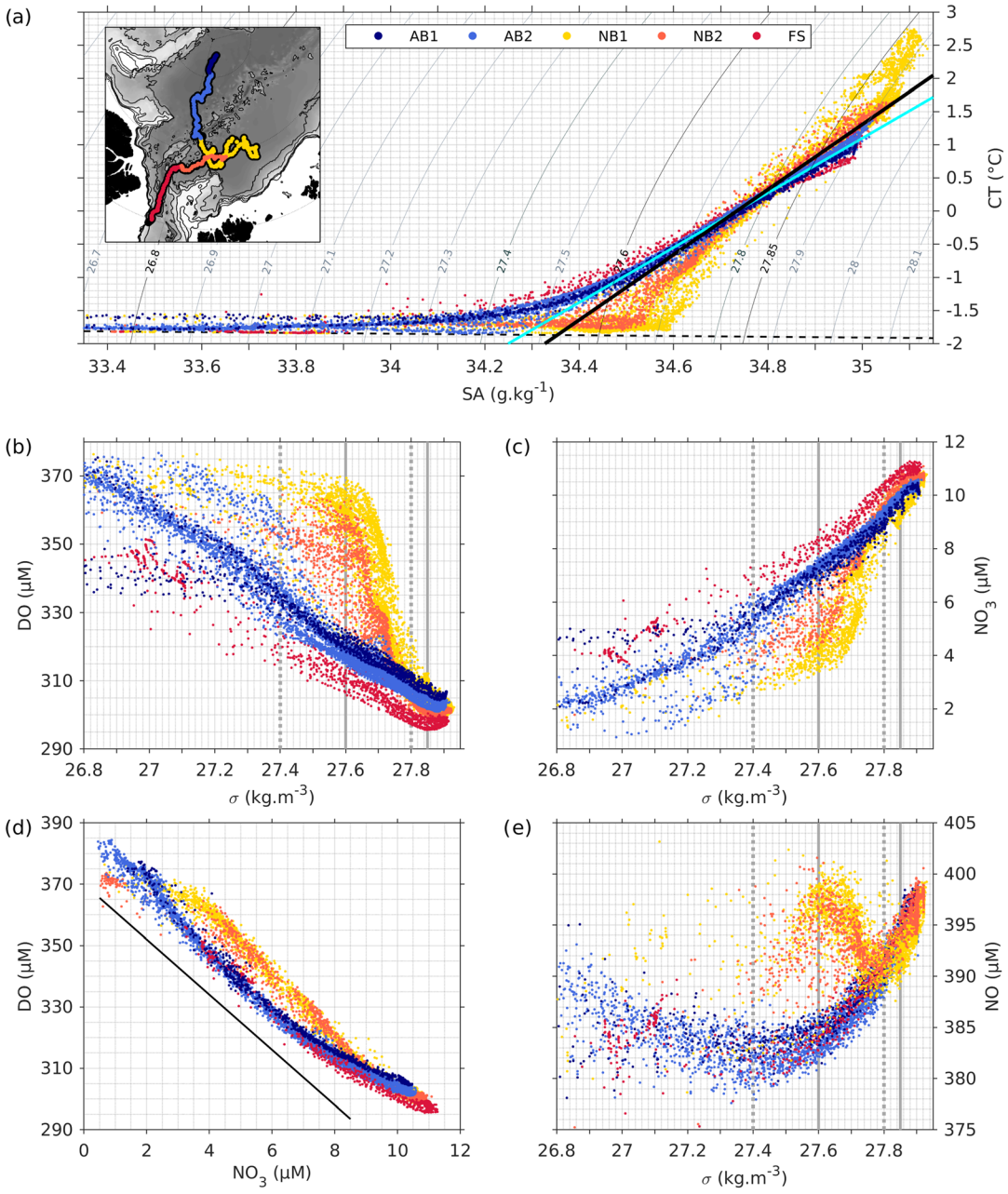

Figure 4. Colors represent regions (Amundsen Basin: AB1 and AB2; Nansen Basin: NB1 and NB2; Fram Strait: FS; and the Transpolar Drift (TPD) corresponds to AB1, AB2, and FS). Diagrams of select variables: (a) CT-SA with two mixing lines, one for TPD (solid line cyan) and the other for Nansen Basin (solid line black); mixing lines are drawn through values of CT and SA at 180- and 250-m depths (following Kikuchi et al., 2004); (b) DO-σ; (c) NO_3-σ; (d) DO-NO_3 where a black line with a slope of −9 is represented; (e) NO-σ. Vertical dotted lines mark densities associated to NO minima (27.4 and 27.8 kg·m^{-3}), and vertical plain lines correspond to bottom of cold and lower halocline densities (27.6 and 27.85 kg·m^{-3}).

2 µM and increased with depth to reach values in excess of 10 µM at σ of 27.85 kg·m^{-3} (SA of 34.9 g·kg^{-1}). The larger DO values in the Nansen Basin in the σ range 27.4–27.8 kg·m^{-3} (yellow and orange dots in Figure 4b) were consistent with recently ventilated waters (Figure 4a) that were relatively depleted in nitrate compared to waters from the TPD (Figure 4c). For a given density, waters in the TPD (blue in Amundsen Basin and red in Fram Strait; Figures 4b–4d) showed a progressive increase in nitrate and decrease in DO.

The DO-NO_3 diagram (Figure 4d) shows that the ratio of DO to nitrate concentrations is close to Redfield stoichiometry in Nansen Basin (orange and yellow dots), except in the upper layer (large DO small NO_3) because of nitrate uptake due to primary production (Boles et al., 2020). In the TPD, the ratio deviated from a straight line (Figure 4d), and this departure reflected in the NO parameter which showed a marked minimum of 380–385 μM at σ values of 27.3–27.6 kg·m^{-3} (Figure 4e). In Nansen Basin, the NO parameter showed a minimum of 390–395 μM at σ values of about 27.8 kg·m^{-3}.

Along the drift, the NO parameter shows a distinct spatial distribution from that of its parent constituents (Figures 2c–2e). Salient features in the NO distribution are the minimum centered on the 27.4 isopycnal in the TPD (Amundsen and Fram Strait) and a weaker minimum centered on the 27.8 isopycnal in Nansen Basin (Figure 2e). Throughout the drift, NO shows values of 390–395 μM on the 27.8 kg·m^{-3} isopycnal which lies at about 110-120 m depth in Nansen Basin and close to 200 m in Amundsen Basin. Abrupt changes in NO above the 27.8 kg·m^{-3} horizon occurred on the southern side of Amundsen Basin and at the exit to Fram Strait with a stark contrast between waters from the TPD (in Amundsen and in Fram Strait; Figure 1a), poorer in DO and NO (leading to NO < 380 μM) than waters below the mixed layer in the upper Nansen Basin (NO > 390 μM). Origins of the NO minima on 27.4 and 27.8 kg·m^{-3} isopycnal horizons (SA = 34.2 and 34.8 g·kg^{-1}) are discussed below.

4. Halocline Structure, Sources, and Strength Along the Drift

4.1. TPD: Halocline Structure and Origin of the NO Minimum at 27.4

Below the SML (H_{SML} is about 45 m) and above isopycnal 27.6 kg·m^{-3} (located at about 120 m depth and highlighted with a thick black line in Figure 5), vertical salinity gradients were large ($\partial_z SA > 1 \times 10^{-2}$ g·kg^{-1}·m^{-1}), and vertical temperature gradients were small ($\partial_z CT < 1 \times 10^{-2}$°C·m^{-1}) (Figures 5a and 5b). The vertical derivative of NO parameter changed sign on the 27.4 σ-isoline corresponding to the NO minimum (Figure 5c). The 70 m-thick layer between the SML and isopycnal 27.6 with SA in the range 33.4 to 34.46 g·kg^{-1}, cold temperatures below −1.5°C and including the NO minimum (Figures 2b and 2d), corresponded the cold halocline layer. Between isopycnals 27.6 and 27.85 kg·m^{-3} (thick black lines in Figure 5), the vertical salinity gradient was small ($0.5 < \partial_z SA < 1 \times 10^{-2}$ g·kg^{-1}·m^{-1}), the vertical temperature gradient was larger ($\partial_z CT > 1.5 \times 10^{-2}$°C·m^{-1}), and vertical NO gradient was positive (>0.1 μM. m^{-1}). We considered that isopycnal 27.85 kg·m^{-3} marked the upper limit of the Atlantic layer (at σ > 27.85 kg·m^{-3}, temperatures were positive above 0.5°C and salinity values above 34.9 g·kg^{-1}) and the lower limit of the lower halocline. Thus, the LHW layer in the TPD in Amundsen Basin lay within isopycnals 27.6 and 27.85 kg·m^{-3} in the salinity range 34.46 to 34.9 g·kg^{-1} and temperature range −1°C to 0.5°C. The LHW layer was about 60 m thick.

Isopycnal 27.4 kg·m^{-3}, associated to the location of the NO minimum in Amundsen Basin (Figure 2e), corresponded to a density ratio R_ρ of 0.05 (Figure 5d), isopycnal 27.6 kg·m^{-3}, the base of the cold halocline there, to an R_ρ of 0.1 and isopycnal 27.85 kg·m^{-3}, the base of the lower halocline, to R_ρ values larger than 0.3 (Figure 5d).

Profiles from 18 June (in blue in Figures 5e–5g) illustrate the vertical structure in the TPD in Amundsen Basin with a NO minimum between 60 and 110 m corresponding to an R_ρ value between 0 and 0.1 and a density between 27.05 and 27.6 kg·m^{-3}.

In an attempt to understand the origin of water parcels in the NO minimum centered on the 27.4 σ-horizon in Amundsen Basin, we performed back trajectories at different depths and starting at different times (every 5 days from 30 April to 30 June) from a box extending from 85°N to 87°N and from 12°W to 12°E (black box in Figures 6a–6c). Back trajectories from the 5 to 70 m depth range consistently suggested contributions from the East Siberian Sea and Laptev Sea continental slopes (Figures 6a and 6b). Advective time scales from the East Siberian Sea slope (~79°N, 165°E) varied with depth (~1 year at 5 m; ~1.5 to 2 years at 70 m). On the other hand, 2-year-long back trajectories at 110 (not shown) and 220 m (Figure 6c) were short and indicated old recirculating Modified AW. These deep trajectories (Figure 6c) were consistent with the low CT and SA observed in the Amundsen Basin Modified AW (Figures 2a, 2b, and 4a).

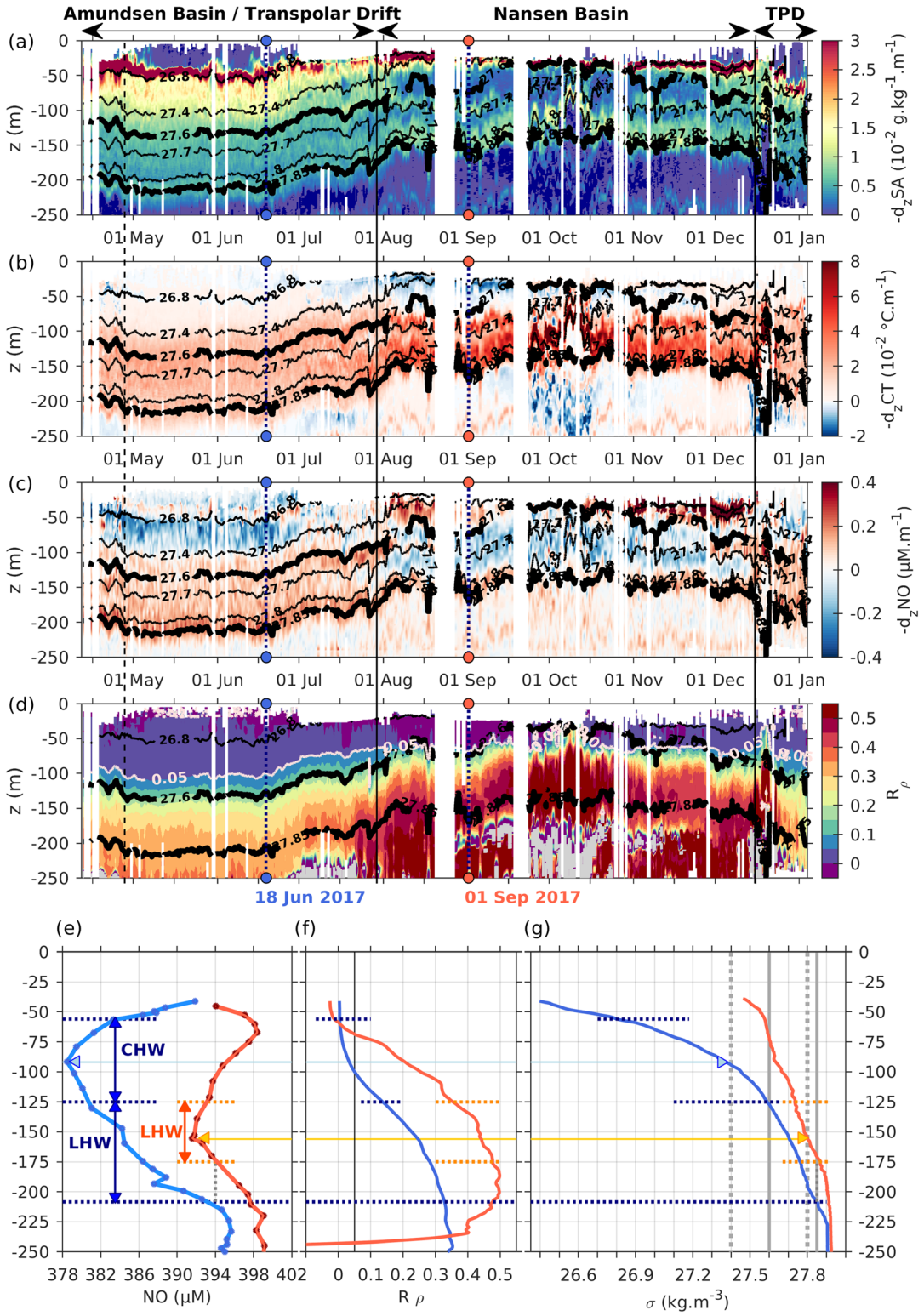

Figure 5. Vertical gradient of variables along the drift trajectory (x axis is time, and y axis is depth): (a) SA (10^{-2} g·kg^{-1}·m^{-1}); (b) CT (10^{-2}°C·m^{-1}); (c) NO (µM·m^{-1}); (d) density ratio R_ρ with isoline 0.05 in white. Isopycnals are in black. Profiles of (e) NO parameter, (f) density ratio R_ρ, and (g) potential density σ in Amundsen Basin on 18 June in blue and in Nansen Basin on 1 September in orange. Black line in (f) marks $R_\rho = 0.05$. Limits of cold halocline (CHW) and lower halocline (LHW) are represented with dotted lines.

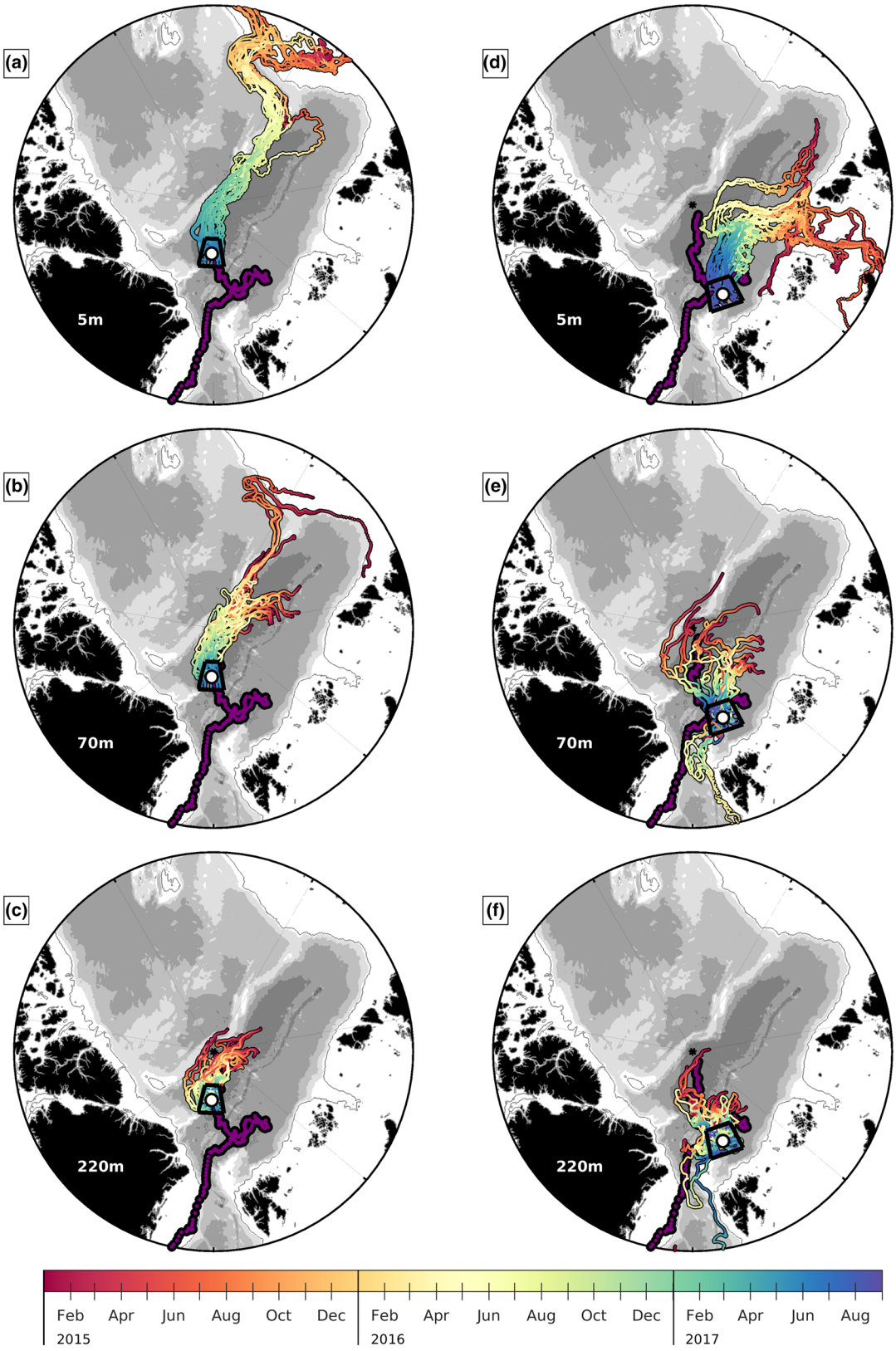

Figure 6. Back trajectories in Amundsen Basin from 18 June 2017 (a–c) at 5, 70, and 220 m depth calculated with PSY4 velocities from a box centered on the location of the NO minimum (85–87°N; 12°W–12°E). Back trajectories in Nansen Basin from 1 September 2017 (d–f) at 5, 70, and 220 m starting in the box (83–85°N; 10–30°E). Color is time.

4.2. Upper Layer Structure in the Nansen Basin

In Nansen Basin (1 August to 19 December), H_{SML} was about 40 m. In contrast with the stratification in the TPD, salinity and temperature vertical gradients below the mixed layer covaried: they were small ($\partial_z SA < 1 \times 10^{-2}$ g·kg^{-1}·m^{-1} and $\partial_z CT < 4 \times 10^{-2}$°C·m−1) down to 27.7 kg·m^{-3} isopycnal depth (Figures 5a and 5b). The vertical NO derivatives changed sign from negative to positive on the 27.8 σ-horizon (in the LHW) which corresponded to a local minimum in NO (Figures 5c and 2e). Profiles from 1 September showed a local minimum in NO (392 μM) at about 150 m on the 27.8 σ-horizon, corresponding to an R_ρ value between 0.4 and 0.5 (Figures 5e–5g, red profiles). The rather small stratification between the base of the mixed layer and the 27.8 σ-horizon suggests a former deep winter mixed layer. Note that the same NO value (about 392 μM) is also found on the same σ-horizon (27.8 kg·m^{-3}) in the TPD in the Amundsen Basin and in Fram Strait (Figure 2e).

Back trajectories were performed from a region well documented by IAOOS23 during its meandering path from the end of July to mid-December (83–85°N;10–30°E) at different depths and starting at different times (every 5 days from 1 August to 15 December) (examples in Figures 6d–6f). Model back trajectories at 5 m suggested contributions from low-salinity shelf waters (Kara and Barents Seas) moving offshore (Figure 6d). This indicated capping with relatively low salinity water. Away from the continental slope and below the near-surface waters, upper layer velocities were small in the Nansen Basin (Figure 3b), and 3-year-long back trajectories were rather short (Figure 6e). Upper layer water parcels had been in the region for several years and could be traced back to the continental slopes in general with time scales equal to or larger than 3 years (not shown).

In the AW layer of the Nansen Basin, model back trajectories indicated contributions from recirculating AW from western Nansen Basin and new AW from Fram Strait (Figure 6f). The contribution of AW from the south (from Yermak Plateau and western Fram Strait) was larger in December than in previous months (not shown). The slight differences observed in the AW characteristics before and after the end of November (yellow and orange dots in Figure 4) could be associated with the circulation change.

4.3. Halocline Strength

The halocline depth H_{halo}, taken as the depth of the 27.85 isopycnal, varied from about 200 m in Amundsen Basin to 150 m in Nansen Basin (Figure 7a). The halocline eddies HE1 and HE2 encountered in Amundsen Basin (Figure 1c) led to a shoaling of the mixed layer there and a deepening of the base of the halocline and resulted in a halocline thickness of 180 m, the largest encountered during the drift. The smallest H_{halo} was encountered above the two AW mesoscale structures AW1 and AW2 crossed in Nansen Basin (Figure 7a). The depth of the cold halocline, that is, the depth of isopycnal 27.6 kg·m^{-3}, was about 120 m in Amundsen Basin. There was no cold halocline in Nansen Basin where the 27.6 kg·m^{-3} isopycnal shoaled to the depth of the mixed layer (~30 m).

Missing density data in the mixed layer were interpolated using an iterative neighboring approach (Figure 7b), and the strength of the halocline layer was estimated with the APE (section 2.2), a measure of stratification over the whole halocline (from isopycnal 27.85 kg·m^{-3} to the surface) and over the cold halocline (from isopycnal 27.6 kg·m^{-3} to the surface) (Figure 7d). The strength of the whole halocline ranged from values above 6×10^4 J·m^{-2} in Amundsen Basin to less than 0.8×10^4 J·m^{-2} in the Nansen Basin (Figure 7e). At the exit of the TPD in Fram Strait, the APE increased to values above Nansen Basin values but still lower than Amundsen Basin values. The strength of the cold halocline was about half that of the whole halocline and zero in Nansen Basin.

For the sake of comparison, we computed APE from the colocalized model density along the drift (Figure 7c). The depths of the 27.85 and 27.6 isopycnals along the drift compared rather well to observations (Figures 7a and 7b). The model was rather good at representing the temperature and salinity fields as shown in Athanase et al. (2019). However, the frontal region between the fresher Canadian waters and saltier Eurasian waters was represented too further west by about 20° at the time of the buoy drift (April–May). This salinity bias translated into a σ difference of 2 kg·m^{-2} in the upper 50 m in the frontal region (Figure 7d). As a result, the maximum difference in APE between model and observations, reached in the frontal region, was about 3×10^4 J·m^{-2} (Figure 7e).

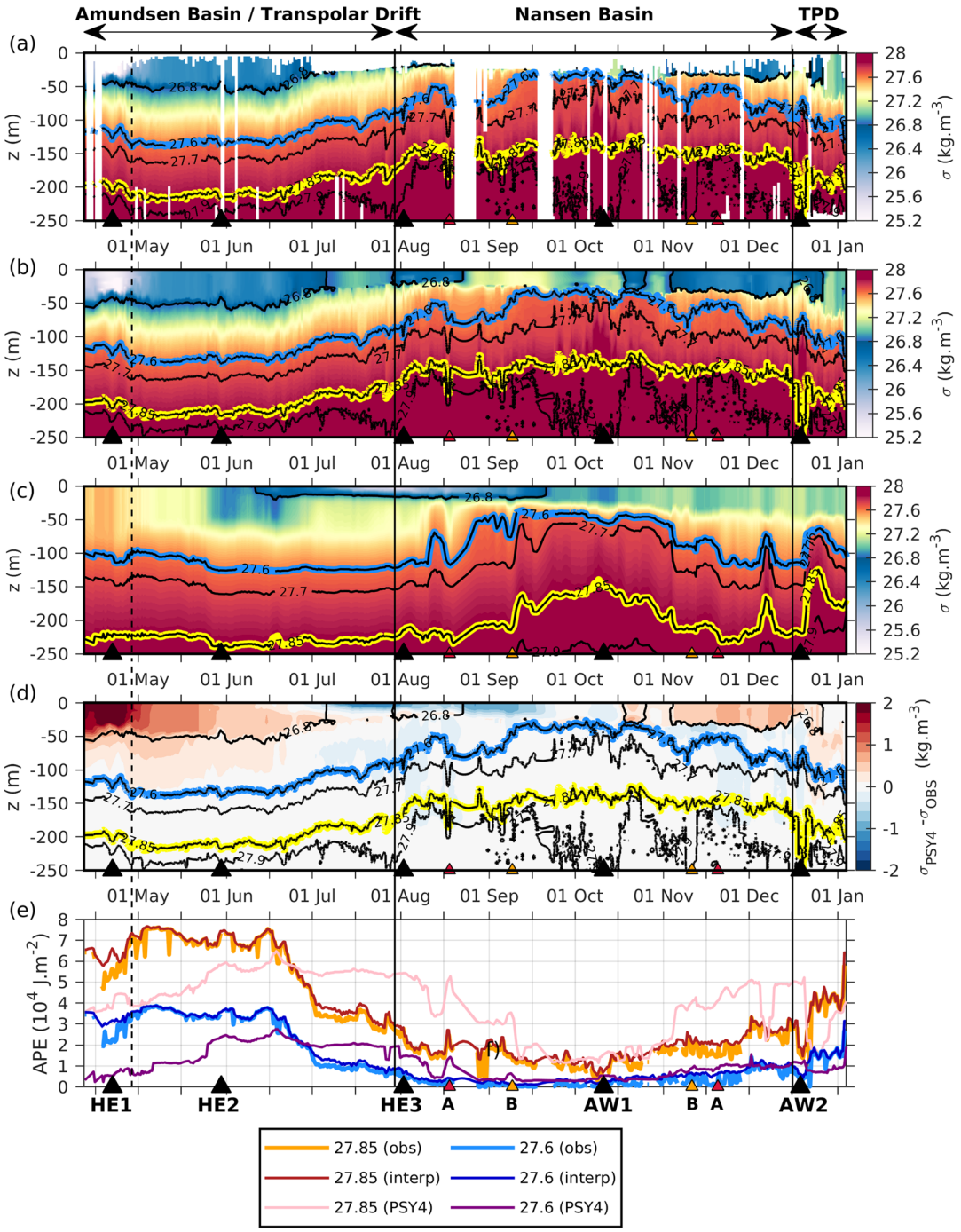

Figure 7. Potential density along the drift trajectory: (a) from observations and (b) from observations interpolated to the surface (c) from PSY4 (*x* axis is time, and *y* axis is depth, isopycnals 27.6 and 27.85 kg·m^{-3} in blue and yellow). (d) Differences between model outputs and observations of potential density. Isopycnals are from observations. (e) Available potential energy (APE, 10^4 J·m^{-2}) calculated from isopycnals 27.85 and 27.6 kg·m^{-3} from observations (orange and light blue), observations interpolated to the surface (red and dark blue) and from PSY4 (pink and purple). Triangles mark positions of halocline eddies (HE1, HE2, and HE3), Atlantic water mesoscale structures (AW1 and AW2), and two crossover points A and B.

The modeled yearly mean APE over the drift region (Figure 8a) provided the spatial distribution of APE over the drift area and showed a maximum difference of less than 2×10^4 J·m^{-2} in the frontal region in the Amundsen region. The modeled mean APE ranged from 0 in the eastern Nansen Basin to 60×10^4 J·m^{-2}

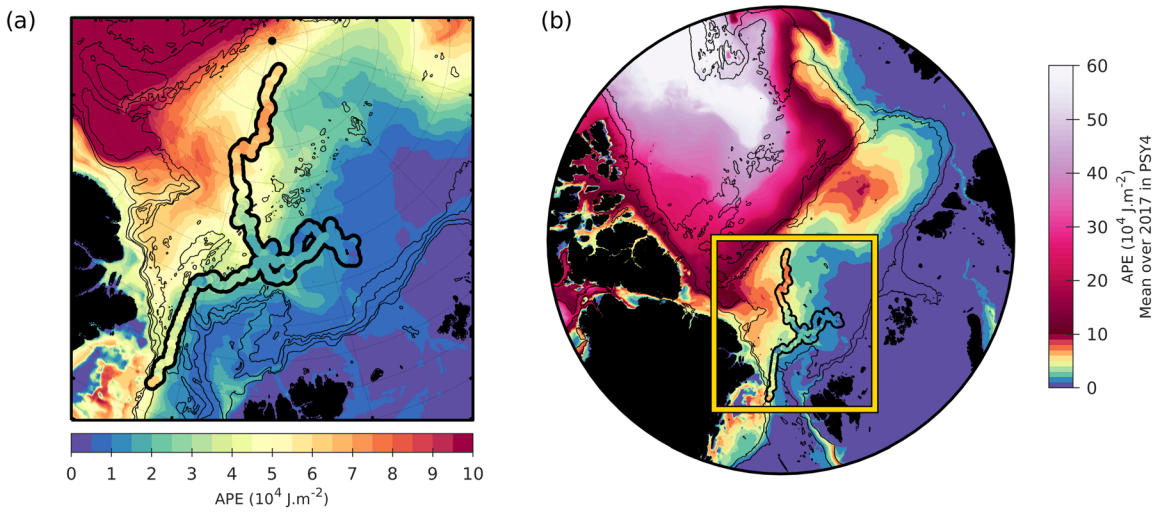

Figure 8. (a) Annual mean model halocline strength (APE from isopycnal 27.85 to the surface) in 2017 and halocline strength along the trajectory from observations. (b) Same as a on a larger Arctic domain.

in the Beaufort gyre region (Figure 8b). The panarctic values are comparable to those estimated in Polyakov et al. (2018). The APE range in the drift area is comparably small (0 to 7 × 10^4 J·m^{-2}).

5. Discussion

5.1. Limitation in NO Estimates and Inferences From Back Trajectories

NO profiles varied over a limited range from 375 to 404 μM compared to the accuracy in NO absolute values in the absence of concomitant bottle data for calibration (cf. Appendix A). However, NO values provided consistent evolution both in time and space (vertical and horizontal) suggesting a high reliability of relative values. It is remarkable that NO values from the TPD in Amundsen and in Fram Strait match each other so well (red and blue dots in Figure 4e) in spite of their differences in NO_3 and DO concentration (Figures 4b and 4c).

While back trajectories should be considered with caution and not over interpreted, they still provide valuable suggestions. Model skills were illustrated through comparisons to IAOOS23 observations (Athanase et al., 2019) with in particular AW1 and AW2 quite well reproduced in characteristics including location and time. However, as no ocean data besides sea ice concentration are assimilated in the ice-covered ocean, we cannot expect mesoscale features to closely match observations in time and space. We performed 2-D back trajectories until January 2014 and obtained consistent results with different starting boxes and different starting times.

5.2. NO Minimum on the 27.8 σ-Horizon

The NO minimum in the LHW (on the 27.8 σ-horizon) in the Nansen Basin (SA of 34.8 g·kg^{-1}, CT about 0°C) is arguably formed with the mechanism initially proposed by Rudels et al. (1996), that is, successive winter deep mixed layers and summer phytoplankton blooms. The upper part of the water column undergoes convective mixing through cooling and brine release during sea ice winter formation creating a winter mixed layer. Later, phytoplankton blooms remove NO_3, and summer temperatures degas the excess DO to the atmosphere. Subsequent winter mixed layer convection homogenizes and replenishes with some (although less and less) nitrate. NO diminishes in the upper layer. Starting with NO_3 concentrations of 6.7 mmol·kg^{-1} and NO value of 408 mmol·kg^{-1} (DO = 350 mmol·kg^{-1}), Rudels et al. (1996) estimated that 3 years were necessary to reach NO values of 385 mmol·kg^{-1} (comparable to the values observed here). Here in Nansen Basin, the stratification is small between the summer mixed layer and the 27.85 σ-horizon. The NO minimum probably lies at the base of a previous deep winter mixed layer.

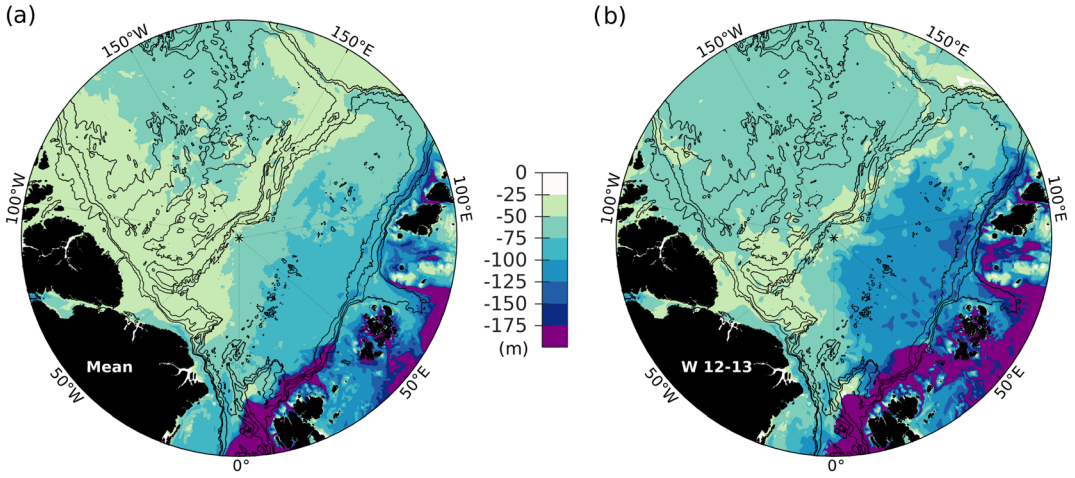

Figure 9. (a) Maxima of winter mixed layer depths from PSY4 averaged over 2007–2017 (in m). (b) Maxima of mixed layer depths during winter 2012–2013.

Over 2007–2017, the modeled winter mixed layers reached depths in excess of 100 m in western Nansen Basin with particularly large values north of Svalbard where winter ventilation often reached deeper than 200 m (Figure 9a). In particular, the model showed wide spread deep mixed layers along the continental slope in winter 2012–2013, with depths similar to those documented at 30°E that winter (e.g., Pérez-Hernández et al., 2019) (Figure 9b). According to the model, these were the deepest winter mixed layers found in that region over the last 10 years. Model results suggested advective pathways from the slope to the inner Nansen Basin in the layer 30–140 m with time scales larger than 3 years (section 4.2). Model mixed layer depths, advective pathways, and time scales were consistent with the observed NO minimum and the NO minimum formation process described by Rudels et al. (1996).

Note that the minimum in NO on the 27.8 σ-horizon corresponds to a local maximum in CDOM (2.4 ppb) below the very low CDOM values in the Nansen Basin halocline (Figure 2f). Nansen Basin halocline is not fed with CDOM-loaded waters from Siberian shelves, and the autochthonous CDOM resulting from primary production is subject to removal processes. There are four major CDOM removal processes: fractionation during sea ice formation, flocculation, microbial degradation, and photochemical degradation (Stedmon et al., 2011). While they are all likely to contribute to the very low CDOM values in the Nansen Basin halocline, their relative importance is uncertain.

5.3. NO Minimum Centered on the 27.4 σ-Horizon

The NO minimum ranging from 375 to 385 μM centered on the 27.4 σ-horizon (around 100-m depth) (Figure 4e) was found at the base of fresh (SA < 33 g·kg^{-1}) waters at close to freezing temperatures with a high CDOM content (CDOM > 3.60 ppb) (Figure 2). The NO minimum was traced back to the slope of the East Siberian Sea with an advective time scale of about 1.5 to 2 years at 70-m depth (Figure 6a). The ocean pathways of Eurasian runoff are modulated by the Arctic Oscillation (Morison et al., 2012). In a period of cyclonic wind regime (positive phase of the Arctic Oscillation), the Siberian runoff is diverted by eastward winds toward the Makarov Basin, and the ocean TPD originates from the East Siberian Seas. Since 2015, a positive Arctic Oscillation index has prevailed (e.g., https://www.cpc.ncep.noaa.gov/products/precip/CWlink/daily_ao_index/month_ao_index.shtml), and the upper ocean mean flow in Mercator Ocean system has shown large velocities from the East Siberian Seas toward the North Pole (e.g., Figures 3a–3c). East Siberian shelf waters have been advected to Amundsen Basin and have been ventilating the Eurasian Arctic Halocline. These waters typically exhibit low NO values because of reduced DO concentrations (Figure 4b) due to remineralization of allochthonous organic matter in both dissolved and particulate forms (Alkire et al., 2010; Alkire et al., 2019; Anderson et al., 2017).

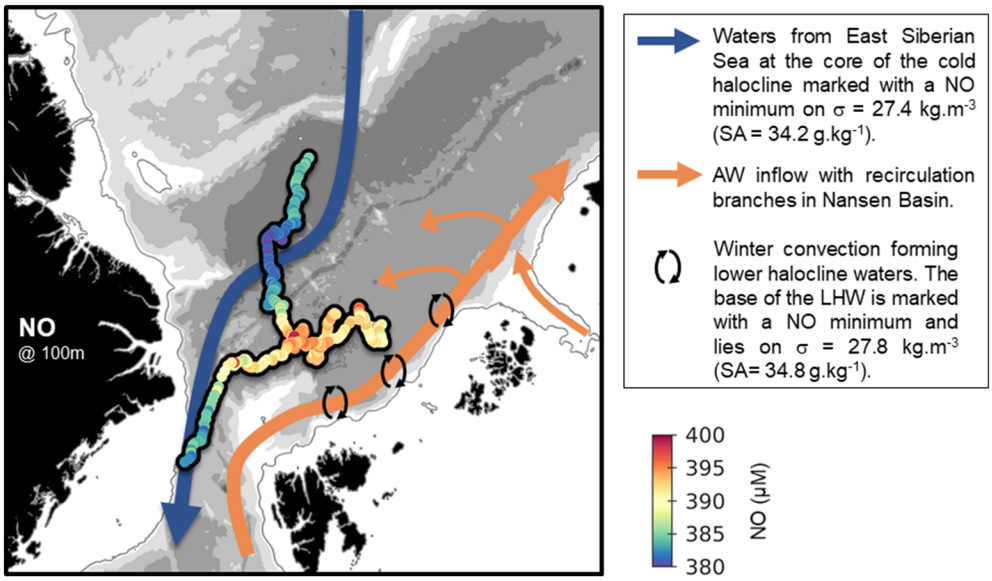

Figure 10. NO concentration at 100 m along the drift and schematics of processes associated with NO distribution. The 100-m depth is close to the core of the cold halocline in Amundsen Basin and to the base of the lower halocline in Nansen Basin (Figure 2e). The NO minimum (380 μM) in the TPD results from advection of low NO waters (depleted in DO) from the East Siberian Seas contributing to the cold halocline on σ-horizon 27.4 (SA = 34.2 g·kg^{-1}). The relatively low NO values (390 μM) in Nansen Basin mark the base of the lower halocline. The lower halocline waters, which are formed through deep convection along the path of the Atlantic water inflow, now reach σ-horizon 27.85 (SA = 34.9 g·kg^{-1}).

5.4. Definition of the Base of the Halocline of LHW in a Period of Atlantification

In section 2.2, we recalled the two criteria that are commonly used for defining the base of the lower halocline: the depth of the 34.3 psu (SA = 34.46 g·kg^{-1}) isohaline (Rudels et al., 1996) and the depth where the density ratio R_ρ reaches 0.05 (Bourgain & Gascard, 2011). Those two criteria are not appropriate anymore to define the base of the lower halocline in a period of strong Atlantification (Polyakov et al., 2017). Winter mixed layers in parts of Nansen Basin now regularly reach 150 m depth (Figures 8a and 8b) and homogenize the water column down to a density of 27.85 kg·m^{-3} and a salinity of 34.9 g·kg^{-1}. Winter mixed layers of 150 m depth or more have been observed along the continental slope at different longitudes (e.g., Pérez-Hernández et al., 2019; Polyakov et al., 2017). Atlantification resulted in a salinification of the mixed layer in Nansen Basin. A more appropriate criterion for H_{halo} would be the depth of the SA = 34.9 g·kg^{-1} isohaline.

The behavior of the density ratio changed from Amundsen Basin to Nansen Basin due to increasing vertical temperature gradients combined with lower vertical salinity gradients in Nansen Basin (Figures 5a, 5b, and 5d). In Nansen Basin, a large range of R_ρ was observed between isopycnals 27.6 and 27.7 kg·m^{-3} ($0 < R_\rho < 0.5$). R_ρ was not an appropriate criterion in Nansen Basin. In the TPD, in Amundsen Basin and Fram Strait, an R_ρ of 0.05 corresponded to the NO minimum and isopycnal 27.4 kg·m^{-3} (Figures 5e–5g).

Our APE estimates were similar to those of Polyakov et al. (2018) in spite of their smaller H_{halo} estimate from using the $R_\rho = 0.05$ criterion. Indeed, if H_{halo} is sensitive to the used criterion, stratification is not, as the most important contributions to APE come from the upper and cold halocline (stratification is weak in LHW). Preliminary accuracy estimates suggest that the model may be a good tool to monitor changes in APE. This needs to be further investigated.

6. Summary and Conclusions

We examined the halocline in the western Eurasian Basin using the first autonomous NO measurements and outputs from an operational physical model. Both approaches were complementary and insightful despite their respective limitations (section 5.1). Figure 10 summarizes our findings.

The IAOOS23 platform was deployed on a floe near the North Pole within the TPD on 12 April 2017. In the TPD, halocline waters comprised waters from the East Siberian Seas and were characterized with a NO minimum of 380 μM on the σ-horizon 27.4 kg·m^{-3} (SA = 34.2 g·kg^{-1}) and high CDOM values (range 3 to 4 ppb). The NO minimum was likely caused by reduced DO concentrations because of remineralization on the shelves, while the large CDOM concentrations resulted from Siberian runoff. The runoff and upper layer ocean pathways were expected from the prevailing positive phase of the Arctic Oscillation (Morison et al., 2012).

The platform left the TPD in August 2017 when winds from the south and from the west pushed the ice toward the east. It then sampled the upper layer from the inner Nansen Basin. Stratification at the base of the summer mixed layer in Nansen Basin was strong due to surface warming and sea ice melt (impeding the profiler to ascend into the mixed layer), and velocities below the summer mixed layer were decoupled from ice drift velocities. The change in stratification, CDOM, and NO at the exit of the TPD was stark: the weak stratification below the summer mixed layer until σ-horizon 27.85 was associated with convective winter mixed layer depths. The LHW convective formation mechanism, called "basin-derived" in Alkire et al. (2017), occurred down to isopycnal 27.85 which was marked with a consistent light NO minimum. The NO minimum at the base of the lower halocline is likely formed according to the coupled biogeochemical process described in Rudels et al. (1996). The depths of the winter mixed layers in Nansen Basin have increased, and the convective layers now reach salinity of 34.9 which marks the limit of the weak lower halocline. The 34.3 psu (SA = 34.46 g·kg^{-1}) isohaline which formerly indicated the base of the lower halocline (Rudels et al., 1996) is now located at the base of the cold halocline (27.6 kg·m^{-3}) in Amundsen Basin.

Autonomous NO measurements were shown to be factible, and conservation of NO parameter at depth was a useful constraint in controlling potential sensor drift (see Appendix A). NO proved to be a useful indicator of halocline structure despite our fragmentary documentation of ocean biogeochemistry in the Arctic. However, a better understanding of Arctic Ocean sources and sinks of nitrate (e.g., Alkire et al., 2019; Chang & Devol, 2009; Gihring et al., 2010) is needed for a quantitative assessment of the halocline water mass composition.

We followed Polyakov et al. (2018) and computed APE as a measure of the strength of the halocline along the drift. The halocline strength was extremely weak in Nansen Basin as a result of Atlantification. Mercator physical system provided reasonable APE estimates. It is important to further assess model skills in monitoring APE in these regions where data gathering requires substantial resources and efforts.

Appendix A: NO_3 and DO Validation and NO Estimates

The ocean profiler on IAOOS23 equipped with a Submersible Ultraviolet Nitrate Analyzer (SUNA) and a DO Aandera 4340 optode was set to perform two profiles a day with measurements on the way up starting from the bottom (250 m).

There was no bottle data and no postdrift calibration as the profiler was lost over shallow topography in Fram Strait. Instrumental drift was evaluated by examining values at 240 m depth and differences at the crossover points visited at different times (e.g., Points A and B in Figure 1a) (see supporting information in Boles et al., 2020). Remarkably little instrumental drift occurred over the 8-month period, except possibly for nitrate concentrations which exhibit a sudden jump of +1.53 ± 0.15 μM on 5 November and return to values prior to the jump by 25 December (Boles et al., 2020). In the absence of contemporaneous bottle data, we used chemistry data from North Pole Earth Observatory (NPEO) from previous years (Falkner et al., 2009) available online (https://arcticdata.io/catalog/view/doi:10.18739/A27H1DK9T).

The SUNA provided both computed nitrate concentrations and absorbance spectra. Nitrate concentrations were recalculated from the spectra using small adjustments in the optical wavelength offset parameter, typically in the range from 206 to 212 nm following the ARGO DAC protocol (Johnson et al., 2018) and compared to the sensor-provided nitrate profiles (SUNA) and to several NPEO profiles (ISUS instrument calibrated with bottle measurements) made in the same area (Figure A1, left panel). The change of the optical wavelength offset parameter led to a shift of nitrate concentrations (Figure A1, left panel). Nitrate concentrations computed with λ = 210 nm were close to those obtained directly from the SUNA sensor. We

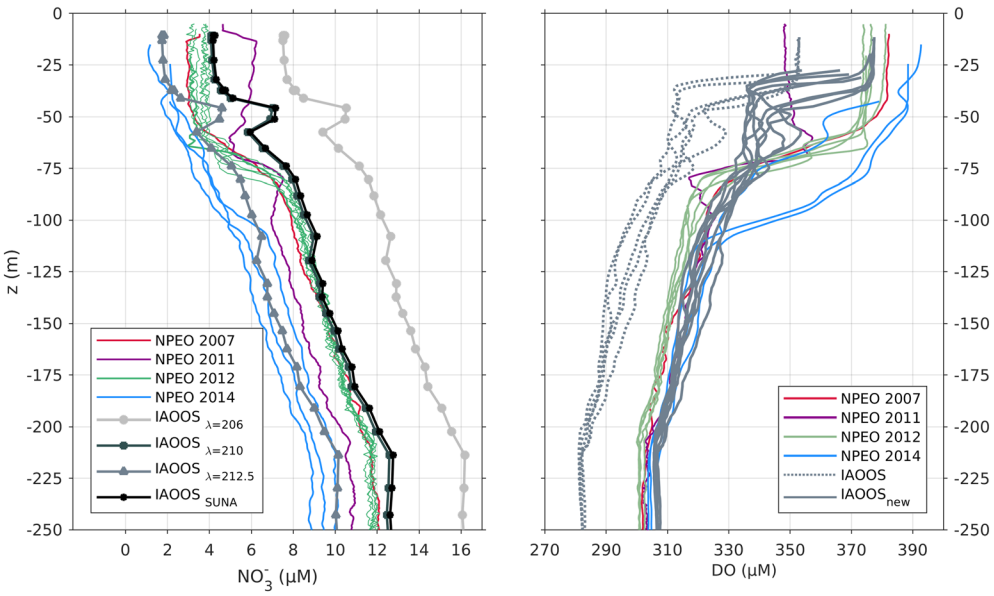

Figure A1. (left) Nitrate concentrations computed from spectrum with three wavelength offsets (206, 210, and 212.5 nm) and directly obtained from SUNA (thick gray and black lines) and from NPEO (ISUS calibrated with bottle measurements) at Barneo site near the North Pole (different years in color) (http://psc.apl.washington.edu/northpole/). (right) Dissolved oxygen concentrations from IAOOS23 in gray (dotted line: raw, solid line: adjusted) and DO from NPEO measurements near the North Pole (different years in color).

chose to use nitrate concentrations computed from spectrum with $\lambda = 212.5$ nm which provided values comparable to NPEO data (Figure A1, left panel).

DO concentrations were retrieved following Thierry et al. (2016). Apparent oxygen utilization (AOU) was computed and compared to AOU derived from DO bottle measurements from NPEO. Comparisons suggested a systematic offset of 25 µM, which was corrected (Athanase et al., 2019). DO concentrations were then recalculated from the corrected AOU (Figure A1, right).

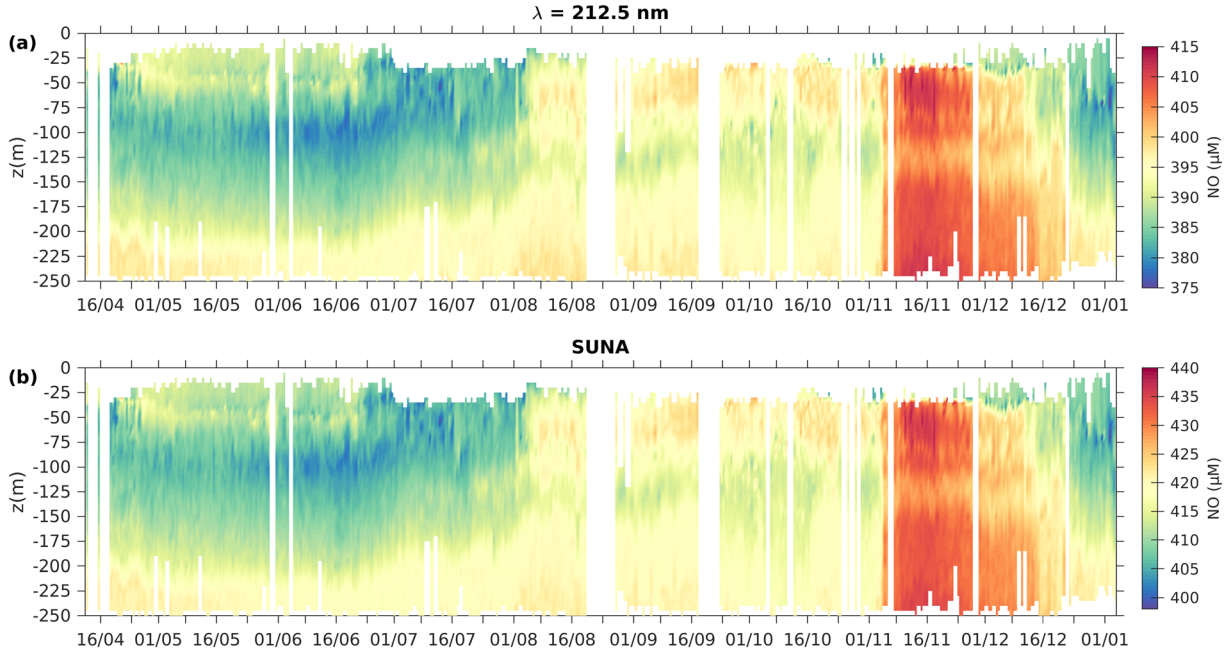

Figure A2. NO parameter along the drift using nitrate concentrations: (a) calculated from spectrum (with a 212.5-nm offset) and (b) from SUNA data. Vertical structure and time evolution do not change. Values are globally shifted by 22 to 25 µM.

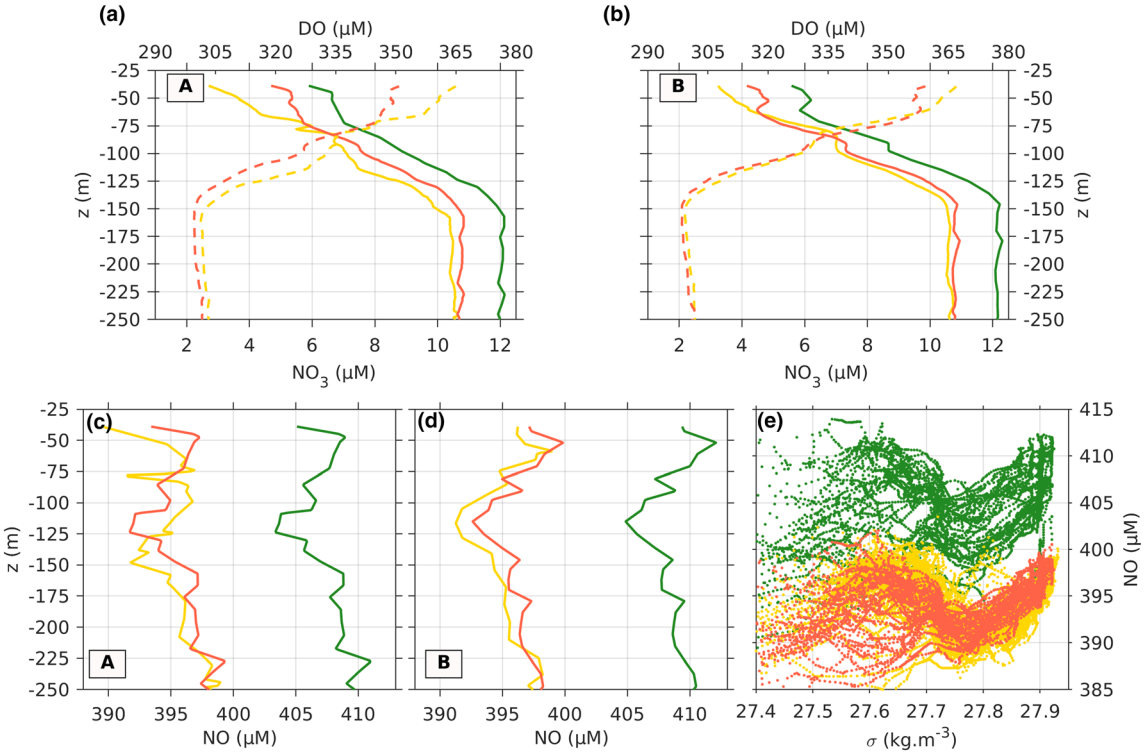

Figure A3. (a) DO (dashed lines) and NO_3 (solid lines) profiles at crossover point A (18 August in yellow and 20 November in green before correction and orange after correction). (b) Same as (a) for the Crossing Point B (9 September and 11 November). (c) NO profiles at Location A on 18 August (yellow) and on 20 November (green before correction and orange after correction). (d) Same as (c) at Location B. (e) NO-σ diagram for all profiles in Nansen Basin between 1 August to 20 December (same color code as Figure 4e) (yellow profiles unchanged and green profiles corrected to orange).

DO and nitrate concentrations were used to compute the NO parameter $NO = 9 \times [NO_3] + [O_2]$. The adjustment for calibration of nitrate and DO concentrations resulted in shifts between 21 and 24 µM in NO which did not change either NO time evolution or NO vertical structure. In particular, the depths of NO minima were conserved (Figure A2).

Boles et al. (2020) suggested that nitrate concentration values after 5 November should be used with caution as they exhibited a sudden jump of $+1.53 \pm 0.15$ µM on 5 November throughout the sampled water column. Nitrate concentration values returned to values prior to the jump after 25 December, after the profiler crossed a swift current associated with a recirculating branch of the West Svalbard Current labeled as AW2 in Figure 1a (Athanase et al., 2019). The nitrate concentration jump from 5 November to 25 December translated into suspiciously large NO values (Figure A2). As large spikes were observed in the backscatter starting in October (Boles et al., 2020), the vertically constant jump (caused by lower absorption values in the SUNA spectra) could be due to an aggregate of sinking algal matter dimming the SUNA window until it was washed away by the strong currents associated with AW2.

We tentatively corrected the NO_3 values during the jump, considering that NO was conserved at depth. The correction is detailed for Points A and B that were sampled two times, before and after the "nitrate jump": A on 18 August and 20 November and B on 9 September and 11 November (Figures 1a, A2, and A3). The corrected NO_3 values (orange solid lines in Figures A3a and A3b) were slightly larger than the nitrate concentration measured during the first crossing (yellow solid lines in Figures A3a and A3b) in agreement with slightly diminished DO concentration (dashed lines in Figures A3a and A3b).

NO parameter conservation at depth was an interesting constraint.

Data Availability Statement

IAOOS23 data and NPEO chemistry data can be found online (10.17882/59183 and https://arcticdata.io/catalog/view/doi:10.18739/A27H1DK9T, respectively).

Acknowledgments

We are deeply grateful to the many people who participated in the development and tests of the biogeochemical profiler at Ifremer facilities in Brest (France) and during the N-ICE 2015 ice camp from RV *Lance* north of Svalbard: Magali Garracio, Antoine Guillot, Christine Drezen, Michel Calzas, Nicolas Villacieros Robineau, Jean-Philippe Savy, and Victoire Rérolle. We thank Zoé Koenig, Matthieu Labaste, Victoire Rérolle, and Sergey Pisarev for their contribution to the preparation and deployment of the IAOOS platforms from the North Pole in April 2017. Magali Garracio was essential to the data recovery and decoding processes. Discussions with Catherine Schmechtig and Paul Dodd on the data processing and Véronique Garçon on the manuscript are gratefully acknowledged. The development and field work were funded through the ANR EQUIPEX IAOOS project through ANR-10-EQX-611 32-01 grant and the ICE-ARC program from the European Union 7th framework programme, Grant 603887. Elisabeth Boles and Marylou Athanase were supported through the Pan Arctic Options Belmont Forum project (ANR-14-AORS-003-01). Cecilia Bertosio was supported through IAOOS Grant S18JROI002 at Sorbonne University.

References

Alkire, M. B., Falkner, K. K., Morison, J., Collier, R. W., Guay, C. K., Desiderio, R. A., et al. (2010). Sensor-based profiles of the NO parameter in the central Arctic and southern Canada Basin: New insights regarding the cold halocline. *Deep Sea Research, Part I*, *57*(11), 1432–1443. https://doi.org/10.1016/j.dsr.2010.07.011

Alkire, M. B., Falkner, K. K., Rigor, I., Steele, M., & Morison, J. (2007). The return of Pacific waters to the upper layers of the central Arctic Ocean. *Deep Sea Research, Part I*, *54*(9), 1509–1529. https://doi.org/10.1016/j.dsr.2007.06.004

Alkire, M. B., Morison, J., & Andersen, R. (2015). Variability and trends in the meteoric water, sea-ice melt, and Pacific water contributions to the central Arctic Ocean, 2000–2013. *Journal of Geophysical Research: Oceans*, *120*, 1573–1598. https://doi.org/10.1002/2014JC010023

Alkire, M. B., Polyakov, I., Rember, R., Ashik, I. M., Ivanov, V., & Pnyushkov, A. V. (2017). Lower halocline water formation and modification, a comparison of physical and geochemical methods. *Ocean Science*, *13*(6), 983–995. https://doi.org/10.5194/os-13-983-2017

Alkire, M. B., Rember, R., & Polyakov, I. (2019). Discrepancy in the identification of the Atlantic/Pacific front in the central Arctic Ocean: NO versus nutrient relationships. *Geophysical Research Letters*, *46*, 3843–3852. https://doi.org/10.1029/2018GL081837

Anderson, L. G., Andersson, P. S., Björk, G., Jones, E. P., Jutterström, S., & Wåhlström, I. (2013). Source and formation of the upper halocline of the Arctic Ocean. *Journal of Geophysical Research: Oceans*, *118*, 410–421. https://doi.org/10.1029/2012JC008291

Anderson, L. G., Björk, G., Holby, O., Jutterström, S., O'Regan, C. M., & Pearce, I. (2017). Shelf-basin interaction along the Laptev-East Siberian Sea. *Ocean Science*, *13*(2), 349–363. https://doi.org/10.5194/os-13-349-2017

Athanase, M., Sennéchael, N., Garric, G., Koenig, Z., Boles, E., & Provost, C. (2019). New hydrographic measurements of the upper Arctic western Eurasian Basin in 2017 reveal fresher mixed layer and shallower warm layer than 2005–2012 climatology. *Journal of Geophysical Research: Oceans*, *124*, 1091–1114. https://doi.org/10.1029/2018JC014701

Boles, E., Provost, C., Garçon, V., Koenig, Z., Bertosio, C., Athanase, M., & Sennéchael, N. (2020). Under-ice phytoplankton blooms in the central Arctic Ocean: Insights from the first biogeochemical IAOOS platform drift in 2017. *Journal of Geophysical Research: Oceans*, *125*, e2019JC015608. https://doi.org/10.1029/2019JC015608

Bourgain, P., & Gascard, J. C. (2011). The Arctic Ocean halocline and its interannual variability from 1997 to 2008. *Deep Sea Research, Part I*, *58*(7), 745–756. https://doi.org/10.1016/j.dsr.2011.05.001

Bourgain, P., Gascard, J. C., Shi, J., & Zhao, J. (2013). Large-scale temperature and salinity changes in the Canadian Basin of the Arctic Ocean at a time of a drastic Arctic Oscillation inversion. *Ocean Science*, *9*(2), 447–460. https://doi.org/10.5194/os-9-447-2013

Broecker, W. S. (1974). "NO": A conservative water mass tracer. *Earth and Planetary Science Letters*, *23*(1), 100–107. https://doi.org/10.1016/0012-821X(74)900036-3

Chang, B., & Devol, A. (2009). Seasonal and spatial patterns of sedimentary denitrification rates in the Chukchi Sea. *Deep Sea Research, Part II*, *56*(17), 1339–1350. https://doi.org/10.1016/j.dsr2.2008.10.024

Falkner, K. K., Collier, R., & Alkire, M. (2009). North Pole Environmental Observatory ISUS nitrate data. Arctic data Center. https://doi.org/10.18739/A27H1DK9T

Fillipi, J.-B., Komatsu, T., & Tanaka, K. (2010). Simulation of drifting seaweeds in East China Sea. *Ecological Informatics*, *5*(1), 67–72. https://doi.org/10.1016/j.ecoinf.2009.08.011

Gihring, T. M., Lavik, G., Kuypers, M. M., & Kostka, J. E. (2010). Direct determination of nitrogen cycling rates and pathways in Arctic fjord sediments (Svalbard, Norway). *Limnology and Oceanography*, *55*(2), 740–752. https://doi.org/10.4319/lo.2010.55.2.0740

Ivanov, V., Smirnov, A., Alexeev, V., Koldunov, N. V., Repina, I., & Semenov, V. (2018). Contribution of convection-induced heat flux to winter ice decay in the western Nansen Basin. *Journal of Geophysical Research: Oceans*, *123*, 6581–6597. https://doi.org/10.1029/2018JC013995

Johnson, K., Pasqueron de Fommervault, O., Serra, R., D'Ortenzio, F., Schmechtig, C., Claustre, H., & Poteau, A. (2018). Processing Bio-Argo nitrate concentration at the DAC Level. Argo data management. https://doi.org/10.13155/46121

Jones, E. P., & Anderson, L. G. (1986). On the origin of the chemical properties of the Arctic Ocean halocline. *Journal of Geophysical Research*, *91*(C9), 10,759–10,767. https://doi.org/10.1029/JC091iC09p10759

Kikuchi, T., Hatakeyama, K., & Morison, J. H. (2004). Distribution of convective lower halocline water in the eastern Arctic Ocean. *Journal of Geophysical Research*, *109*, C12030. https://doi.org/10.1029/2003JC002223

Kipp, L. E., Charette, M. A., Moore, W. S., Henderson, P. B., & Rigor, I. G. (2018). Increased fluxes of shelf-derived materials to the central Arctic Ocean. *Science Advances*, *4*(1), eaaO1302. https://doi.org/10.1126/sciadv.aao1302

Koenig, Z., Provost, C., Sennéchael, N., Garric, G., & Gascard, J. C. (2017). The Yermak Pass Branch: A major pathway for the Atlantic water north of Svalbard? *Journal of Geophysical Research: Oceans*, *122*, 9332–9349. https://doi.org/10.1002/2017JC013271

Koenig, Z., Provost, C., Villacieros-Robineau, N., Sennéchael, N., Meyer, A., Lellouche, J.-M., & Garric, G. (2017). Atlantic waters inflow north of Svalbard: Insights from IAOOS observations and Mercator Ocean global operational system duringN-ICE2015. *Journal of Geophysical Research: Oceans*, *122*, 1254–1273. https://doi.org/10.1002/2016JC012424

Lellouche, J. M., Greiner, E., Le Galloudec, O., Garric, G., Regnier, C., Drévillon, M., et al. (2018). Recent updates on the Copernicus Marine Service global ocean monitoring and forecasting real-time 1/12° high resolution system. *Ocean Science*, *14*(5), 1093–1126. https://doi.org/10.5194/os-14-1093-2018

Morison, J., Kwok, R., Peralta-Ferriz, C., Alkire, M., Rigor, I., Andersen, R., & Steele, M. (2012). Changing Arctic Ocean freshwater pathways. *Nature*, *481*(7379), 66–70. https://doi.org/10.1038/nature10705

Pérez-Hernández, M. D., Pickart, R. S., Torres, D. J., Bahr, F., Sundfjord, A., Ingvaldsen, R., et al. (2019). Structure, transport, and seasonality of the Atlantic water boundary current north of Svalbard: Results from a yearlong mooring array. *Journal of Geophysical Research: Oceans*, *124*, 1679–1698. https://doi.org/10.1029/2018JC014759

Polyakov, I. V., Pnyushkov, A. V., & Carmack, E. C. (2018). Stability of the Arctic halocline: A new indicator of arctic climate change. *Environmental Research Letters*, *13*(12), 125,008. https://doi.org/10.1088/1748-9326/aaecle

Polyakov, I. V., Pnyuskov, A. V., Alkire, M. B., Ashik, I. M., Baumann, T. M., Carmack, E. C., et al. (2017). Greater role for Atlantic inflows on sea ice loss in the Eurasian Basin of the Arctic Ocean. *Science*, *356*(6335), 285–291. https://doi.org/10.1126/science.aai8204

Provost, C., Sennéchael, N., Garçon, V., Boles, E., Athanase, M., Koenig, Z., & Labaste, M. (2017). Arctic western Eurasian Basin: IAOOS 23 physical and biogeochemical profiles in 2017. *SEANOE*. https://doi.org/10.17882/59183

Rudels, B., Anderson, L. G., & Jones, E. P. (1996). Formation and evolution of the surface mixed layer and halocline of the Arctic Ocean. *Journal of Geophysical Research*, *101*(C4), 8807–8821. https://doi.org/10.1029/96JC00143

Rudels, B., Jones, E. P., Schauer, U., & Eriksson, P. (2004). Arctic sources of the Arctic Ocean surface and halocline waters. *Polar Research*, *23*(2), 181–208. https://doi.org/10.1111/j.1751-8369.2004.tb00007.x

Shimada, K., Itoh, M., Nishino, S., McLaughlin, F., Carmack, E., & Proshutinsky, A. (2005). Halocline structure in the Canada Basin of the Arctic Ocean. *Geophysical Research Letters*, *32*, L03605. https://doi.org/10.1029/2004GL021358

Stedmon, C. A., Amon, R. M. W., Rinehart, A. J., & Walker, S. A. (2011). The supply and characteristic of Colored dissolved organic matter (CDOM) in the Arctic Ocean: Pan Arctic trends and differences. *Marine Chemistry*, *124*(1-4), 108–118. https://doi.org/10.1016/j.marchem.2010.12.007

Steele, M., & Boyd, T. (1998). Retreat of the cold halocline layer in the Arctic Ocean. *Journal of Geophysical Research*, *103*(C5), 10,419–10,435. https://doi.org/10.1029/98JC00580

Steele, M., Morison, J., Ermold, W., Rigor, I., Ortmeyer, M., & Shimada, K. (2004). Circulation of summer Pacific halocline water in the Arctic Ocean. *Journal of Geophysical Research: Oceans*, *109*, C02027. https://doi.org/10.1029/2003JC002009

Thierry, V., Bittig, H., Gilbert, D., Kobayashi, T., Sato, K., & Schmid, C. (2016). Processing Argo OXYGEN data at the DAC level, v2.2. https://doi.org/10.13155/39795

Timmermans, M.-L., Marshall, J., Proshutinsky, A., & Scott, J. (2017). Seasonally derived components of the Canadian Basin halocline. *Geophysical Research Letters*, *44*, 5008–5015. https://doi.org/10.1002/2017GL073042